A numerical analysis of transport phenomena in a banded solid oxide fuel cell stack

Karol Śreniawski[a], Marcin Moździerz[b], Grzegorz Brus[c], Janusz S. Szmyd[d]

[a] AGH University of Science and Technology, Krakow, Poland, sreniawski@agh.edu.pl
[b] AGH University of Science and Technology, Krakow, Poland, marcinm@agh.edu.pl
[c] AGH University of Science and Technology, Krakow, Poland, brus@agh.edu.pl
[d] AGH University of Science and Technology, Krakow, Poland, janusz.szmyd@agh.edu.pl

Abstract:

Solid oxide fuel cells (SOFCs) are being recognized as one of the promising energy conversion technologies. To study SOFCs systems operation, numerical modeling is a helpful tool, which allows one to understand and improve their operation. Moreover, a crucial feature of numerical modeling is the opportunity to reduce economical and time cost in prototyping methodology. In this work, a banded SOFC stack, which includes six 12 mm x 12 mm cells, connected in series, applied on a single electrolyte support, is studied numerically, using the finite-volume method. A mathematical model, which includes the heat, mass and electron/ion transport phenomena, was provided. To validate the model, a comparison of electrical characteristics obtained from the numerical and experimental study was performed. To inspect the possibilities of applying geometrical improvements to the existing prototype design, different versions of fuel and air channels were numerically modeled and inspected, including the option of extending the system into two or more stacks, connected by a shared fuel channel of two adjacent stacks. Moreover, the influence of the electrolyte thickness was tested. The proposed design modifications enhance the system by reducing the volume of the stack and improving the electric performance compared to the existing prototype design. The numerical model can be used to test further design modifications to the stack, including performance analysis by changing the operating parameters of the system and applying new materials.

Keywords:

Banded SOFC stack, Hydrogen Use in Energy Systems, Numerical Analysis, Solid Oxide Fuel Cell, Transport Phenomena.

1. Introduction

The use of hydrogen in energy systems is one of the promising and ecologically friendly ways to develop the energy and transport industry. To efficiently convert the chemical energy of hydrogen directly into electrical energy, fuel cells are often utilized. Solid Oxide Fuel Cells (SOFCs) are one of the most efficient fuel cells, with a low manufacturing price compared to other types of fuel cells and a wide range of systems power scale, recognized as the most advanced power generation systems, characterized by the highest thermal efficiency [1]. The prototyping of SOFCs is a highly complex process that involves many costs and time consumption. To reduce these factors, numerical modeling is often used.

Numerical modeling of Solid Oxide Fuel Cells is being recognized as a highly complex but helpful tool in order to better understand the operation and phenomena occurring inside the stack. Many different tools are used for the numerical modeling of SOFCs, while ANSYS Fluent forms one of the most popular and widely used [2]. Three-dimensional numerical modeling of SOFCs is often applied to simulate single-cell operation [3–6], as well as entire stacks [7–9]. 3D SOFC stack simulation was performed successfully by Wei et al. [7], using numerical modeling to study a novel stack arrangement and verify the new shape of the flow channel. The model allowed to observe the thermal stresses in the stack, as well as conduct a transport phenomena verification. To verify the results of the study, a comparison with the results found in the literature was presented. Wei et al. [7] has presented the geometry of the anode-supported planar SOFC stack, which consists of square cells connected electronically using metal interconnectors with ribs, which contribute fuel and air channels. The analyzed geometry of cells is conventional in SOFC systems, also in commercial usage. A proposed multistacking method introduces the original shape of interconnectors. Another interesting approach to the numerical modeling of the SOFC stack was demonstrated by Dong et al. [8]. An anode-supported, five planar, rounded cells stack was modeled. The cells were connected into a stack using nickel and crofer meshes, closed between the outer plates and separators, sealed with mica and the separators. Again, the alignment of cells is one on another. Dong et al. [8] presented the study of the flow uniformity and transport processes inside the stack. The research was also focused on the temperature distribution and electron transport. The

results were compared to the experimental study to demonstrate the correctness of the numerical model. The influence of system size and stack design in terms of flow arrangement was also examined by Pirasaci [9]. Research included the verification of the model by comparing with the results found in the literature. The commercial CFD package, ANSYS Fluent was used in order to simulate the behavior of different design options and study the influence of implemented modifications on the performance of the stack. The analyzed stack geometry is conventional and widely used in commercial systems with rectangular cells closed between metal interconnectors.

Solid Oxide Fuel Cells could also operate using alternative fuels, such as hydrocarbons, ammonia, and carbon monoxide. Due to the high temperature operation, the resistance to impurities in the fuel is elevated [13]. To better understand the processes during operation with alternative fuels, the numerical simulation of single cell SOFCs is also widely used [5,6].

As shown in the literature review, most research focus on conventional stack designs with one on another single cells arrangement, connected using metal interconnectors in different shapes. When comparing our stack design with common SOFC stacks, the originality is clearly visible. Separate electrodes banded on a single electrolyte contribute the novel and original stack arrangement in SOFC systems subject. Moreover, the presented stack banded on the single electrolyte could significantly increase the output voltage, even in small-size systems. The studied design, introduced in [10], also consists of unusual flow channels and electrical connections. Because this paper discusses the impact of channel geometry on the transport phenomena within the recently proposed banded solid oxide fuel cell stack, the electrical connections were simplified. This study focuses on possible improvements in geometry and stack arrangement options. The developed computational fluid dynamic simulation considers momentum, heat, mass, electron and ion transport phenomena.

2. Geometry description
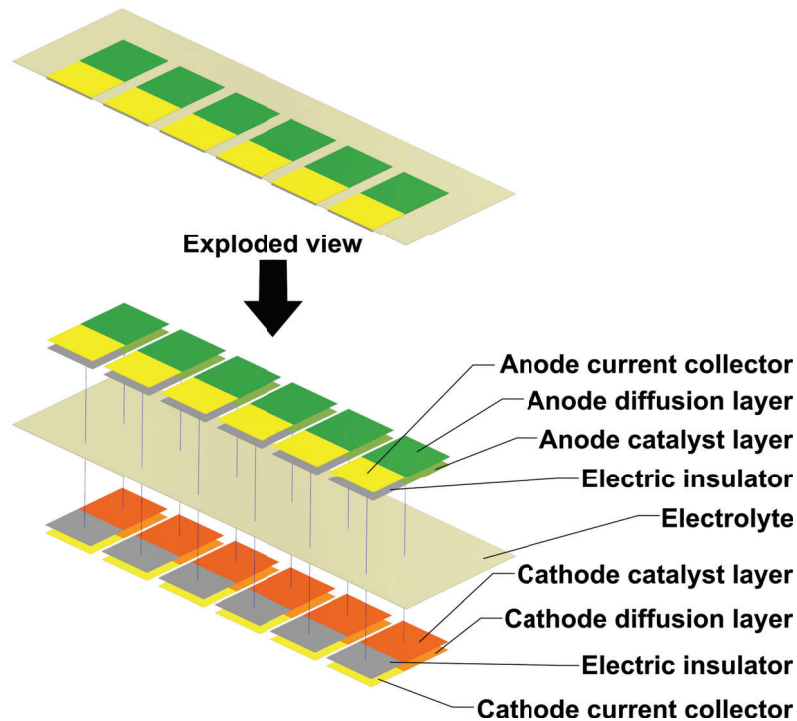
Figure 1: Investigated SOFC stack design with exploded view.

The studied SOFC stack is a novel, patented design [10], which prototype was successfully built and tested [11]. For further development of the stack, a numerical modeling method is used. To prepare a 3-dimensional (3D) numerical model, a computational domain has to be created. Using Autodesk Inventor software, a stack CAD model was created. The stack model, shown in Fig. 1, is composed of six pairs of 12 mm x 12 mm x 0.1 mm electrodes, banded on a single 105 mm x 30 mm x 0.3 mm electrolyte support. Electrolyte support provides high strength and durability of the stack, while maintaining a low production cost [12]. In this paper, the electrolyte of 0.1 mm of thickness is also investigated. The electrodes are divided into two bodies, contributing

catalyst and diffusion layers, as needed for numerical simulation. To simplify the geometry, current collectors are modeled as non-porous solid bodies with side contact to electrodes. Between the electrolyte and the current collectors, electric insulators were applied. Fig. 1 presents the stack assembly, and also to better visualize the model, an exploded view with descriptions was provided.
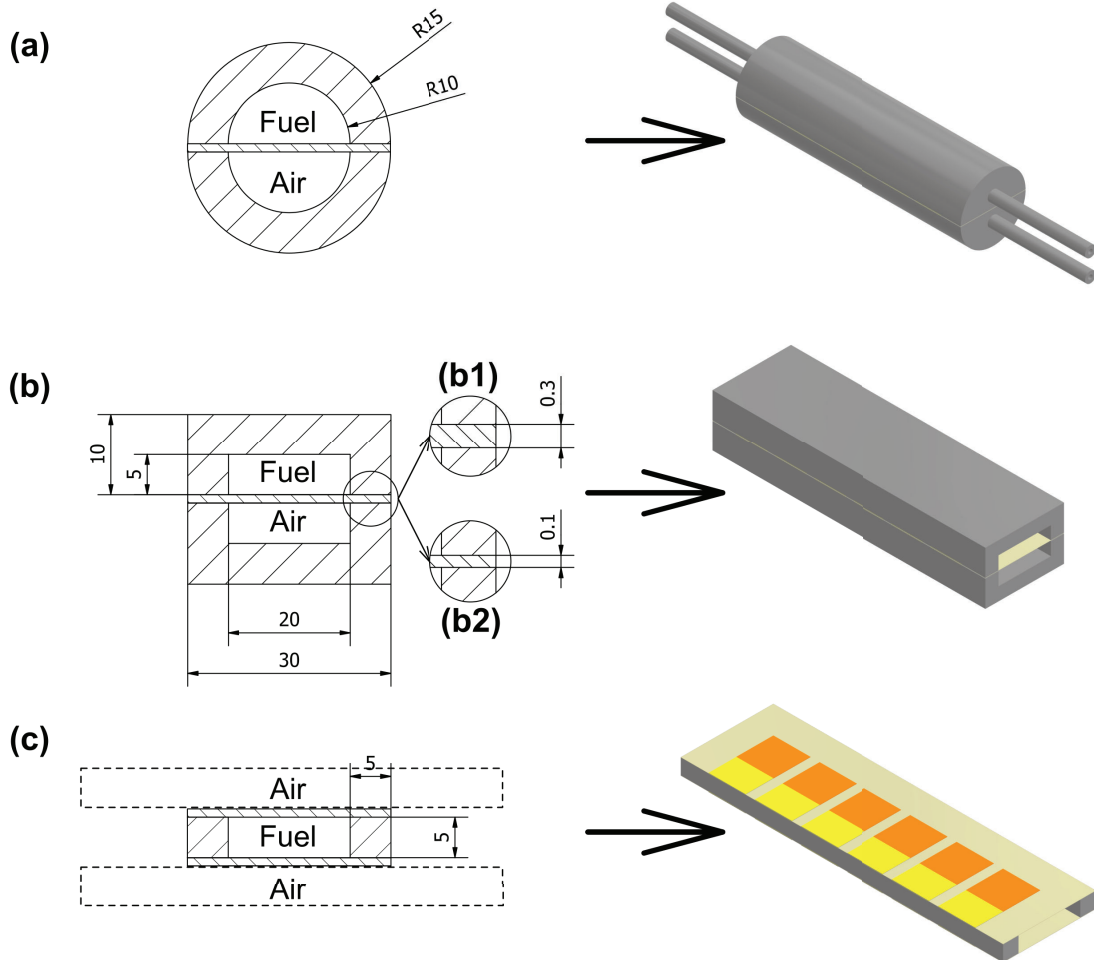
Figure 2: Stack configuration options with schematic cross-sections. Stack supported on 0.3 mm of electrolyte thickness, closed in half-tubular covers, marked (a). The stack with rectangular covers marked (b) comes in two versions: 0.3 mm of electrolyte thickness, marked as (b1), and 0.1 mm of electrolyte thickness, marked (b2). Multi-stack composition with 0.1 mm of electrolyte thickness, marked as (c).

The initial prototype design of the stack includes two ceramic covers, which contribute gases supply elements. During the investigation, a different covers shape and stack arrangement was provided, as shown in Fig. 2, which is divided into three sections. In the (a) section of Fig. 2, the electrolyte support of 0.3 mm of thickness, with deposited cells and the applied current collectors, is enclosed by two half-tubular covers, which state the fuel and air channels, as in the initial design. The (b) section of Fig. 2 presents a rectangular shape of the covers, which was modeled to reduce the stack volume and simultaneously increase the volumetric power density. Moreover, the (b) section was divided into two options. The section marked (b1) is the (b) design supported on 0.3 mm electrolyte, while (b2) is the (b) design supported on 0.1 mm electrolyte. In Fig. 2, the (c) section provides a new idea of extending the system into two or more stacks. By combining two stacks, of which anodes are targeted face to face, a fuel channel is created, while cathodes facing the outer sides could be supplied in the air without an air channel, using a fan. This case consists of two stacks supported on 0.1 mm of electrolyte thickness. This design allows to reduce the volume of the stack even more, and theoretically double the power. To better illustrate each design, schematic cross sections and 3D models were included, respectively. The cross sections demonstrate the arrangement of the stack(s) and covers that

determine the gases paths. This paper also includes a numerical verification of the influence of electrolyte thickness on stack performance, by comparing designs (b1) and (b2).

3. Mathematical model

The mathematical model contains a description of transport phenomena, using a set of partial differential equations. To simplify the model and focus on the demanded areas of physics, a few assumptions were contributed. The model assumes steady state behavior of the operation, the incompressible characteristics of fluids. The energy dissipation and gravitation were ignored. Flow in fluid and porous areas is described as laminar, and all fluids are treated as Newtonian ones.

Steady-state mass conservation equation is used to describe the mass transport in fluid and porous areas, written as follows [8]:

$$\vec{\nabla} \cdot \left(\rho \varepsilon \vec{v} \right) = S_\text{p}, \tag{1}$$

where S_p (kg m^{-3} s^{-1}) represents the source term of mass, as a result of reactants consumed and produced in electrodes through the electrochemical reactions in SOFC. In areas other than porous anodes and cathodes $S_\text{p} = 0$ and $\varepsilon = 1$ (-), which is the porosity rate. In the fluid areas, an equation that describes the conservation of momentum is solved as follows [8]:

$$\vec{\nabla} \cdot \left(\rho \vec{v} \vec{v} \right) = -\vec{\nabla} p + \vec{\nabla} \vec{\vec{\tau}} + \vec{S}, \tag{2}$$

where $\vec{S}$ (kg m^{-2} s^{-2}) is the source term, that describes the viscous and inertial pressure drop.

In porous and fluid areas, the species conservation equation describes the components of the gas mixture, given as follows [8]:

$$\vec{\nabla} \cdot \left(\rho \varepsilon \vec{v} Y_i \right) = -\vec{\nabla} \cdot \vec{J}_{i,\text{eff}} + S_i, \tag{3}$$

where S_i (kg m^{-3} s^{-1}) represents the source and sink terms of species rates, written as follows [8]:

$$S_\text{O}_2 = -\frac{j}{4F} M_\text{O}_2, \tag{4a}$$

$$S_\text{H}_2 = -\frac{j}{2F} M_\text{H}_2, \tag{4b}$$

$$S_\text{H}_2\text{O} = \frac{j}{2F} M_\text{H}_2\text{O}. \tag{4c}$$

The electrons and ions transport potential equations, are given as [3]:

$$\vec{\nabla} \cdot \left(\sigma_\text{el} \vec{\nabla} \phi_\text{el} \right) + j = 0, \tag{5a}$$

$$\vec{\nabla} \cdot \left(\sigma_\text{ion} \vec{\nabla} \phi_\text{ion} \right) + j = 0, \tag{5b}$$

where j (A m^{-3}), the volumetric transfer current density, for the electrons transport on the anode side $j = -j_\text{an}$ and on the cathode side $j = +j_\text{cat}$, and for the ions transport $j = +j_\text{an}$ and $j = -j_\text{cat}$. The volumetric transfer current density j is described by the Butler-Volmer equation, written for the anode and the cathode side as follows [3]:

$$j_\text{an} = \left(\zeta_\text{TPB} i_\text{an}^\text{eq} \right) \left(\frac{X_\text{H}_2}{X_\text{H}_2,\text{ref}} \right)^{\gamma_\text{an}} \left(e^{\alpha_\text{an}^\text{a} F \eta_\text{an}/(RT)} - e^{-\alpha_\text{an}^\text{c} F \eta_\text{an}/(RT)} \right), \tag{6a}$$

$$j_\text{cat} = \left(\zeta_\text{DPB} i_\text{cat}^\text{eq} \right) \left(\frac{X_\text{O}_2}{X_\text{O}_2,\text{ref}} \right)^{\gamma_\text{cat}} \left(e^{-\alpha_\text{cat}^\text{c} F \eta_\text{cat}/(RT)} - e^{\alpha_\text{cat}^\text{a} F \eta_\text{cat}/(RT)} \right). \tag{6b}$$

The local surface overpotential η (V), for the anode and cathode side is given in the following form [3]:

$$\eta_\text{an} = \phi_\text{el} - \phi_\text{ion}, \tag{7a}$$
$$\eta_\text{cat} = \phi_\text{el} - \phi_\text{ion} - \phi_\text{OCV}, \tag{7b}$$

where ϕ_OCV (V) represents the open-circuit voltage.

The heat transport in solid zones is described as the steady-state energy equation, written in the following form [8]:

$$\vec{\nabla} \cdot \left(\varepsilon \vec{v} \rho h \right) = \vec{\nabla} \cdot \left(\left(\varepsilon k_\text{eff} + (1 - \varepsilon) k_\text{s} \right) \vec{\nabla} T - \sum_i h_i \vec{J}_i \right) + S_\text{h}, \tag{8}$$
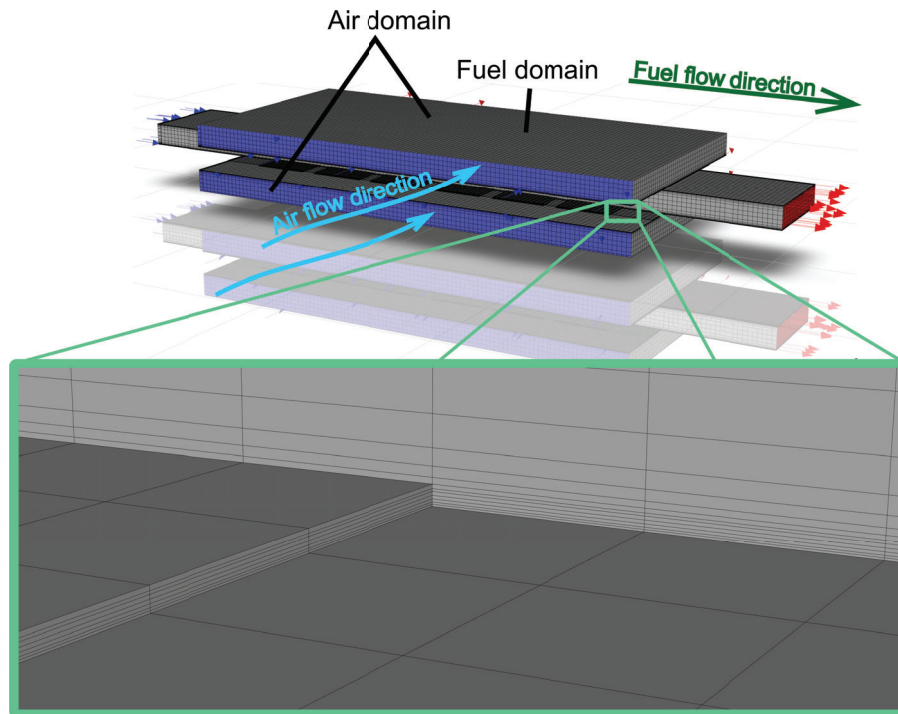
where S_h ($\mathrm{W\,m^{-3}}$) is the total heat source. The heat source in the catalyst layers of electrodes and the electrolyte and is calculated as follows [8]:

$$S_h = -\frac{jh_{\mathrm{react}}}{2F} + j\eta + \frac{i^2}{\sigma}.$$

(9)

In fluid zones, the steady-state energy equation is given in the following form [8]:

$$\vec{\nabla} \cdot (\vec{v}\rho h) = \vec{\nabla} \cdot \left(k_{\mathrm{eff}} \vec{\nabla} T - \sum_i h_i \vec{J_i} \right).$$

(10)

4. Numerical analysis

Figure 3: Visualization of computational mesh of multi-stack design with detailed view.

After the described mathematical model was determined, a series of 3D numerical simulations was performed using the finite-volume method. For the finite-volume method, a computational mesh must be made. To build the mesh of each design described in Section 2., the 3D models were modified to include bodies that represent the paths of the gases. To reduce the number of mesh elements, ceramic covers were removed from the geometries and replaced by the boundary conditions, which represent the behavior of the furnace maintaining constant temperature. Each mesh was created as a compromise between quality and the number of elements, which determined resolution, accuracy, and computational time. The mesh sensitivity study was performed for four different mesh sizes for the initial design marked as (a) in Fig. 2, starting from the number of elements of $1.6 \cdot 10^5$, through $6 \cdot 10^5$, $1.1 \cdot 10^6$ on $4 \cdot 10^6$ of the mesh elements ending. The measured time per iteration was: 1.05 s, 2.14 s; 3.68 s; 17.45 s, respectively. Since the mass conservation for each case remained values under 10^{-8} $\mathrm{kg\,s^{-1}}$, and the electric characteristics did not change, the chosen mesh was the $1.1 \cdot 10^6$ of the elements one. As a result of the large difference in scale between the thin layers of the stack area and the gases domains, a smooth transition of element sizing was applied. Each mesh was built using hexahedral elements. The main mesh element was determined as a 1 mm x 1 mm x 1 mm cube. In the stack area, elements are flattened up to 0.01 mm to retain a minimum of three layers per body in the thickness direction, to then inflate smoothly in the gases areas to main dimensions. In Fig. 3, a computational mesh of multi-stack design, shown in Fig. 2(c), is illustrated, including the detailed view in the zoom box, which shows the inflation of elements thickness in the area of the solid and fluid zones contact. Other designs computational meshes are consistent with the illustrated one.
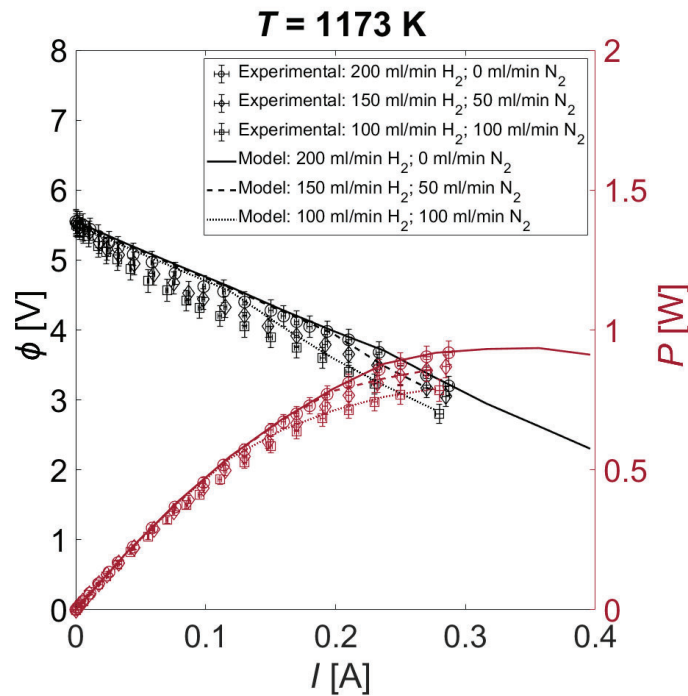
Figure 4: Comparison of current-voltage and current-power characteristics of initial design ((a) in Fig. 2), obtained from numerical analysis and experimental study [11]. Flow rates fitted to tested ones.
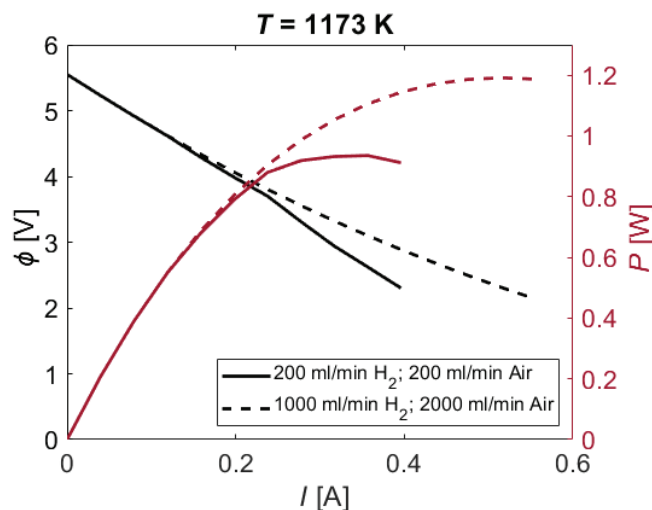
Figure 5: Comparison of current-voltage and current-power characteristics of initial design ((a) in Fig. 2) for different flow rates.

To make an accurate comparison of each investigated design, boundary conditions were retained in all simulations, as well as electrochemical, material, and operating parameters determined for the initial design. To simulate the behavior of the furnace interior and substitute the ceramic covers, constant temperature and zero species flux boundary conditions at the outer walls of the fluid domains were established. On the outer walls of the solids, no current leakage was allowed, except current collectors taps. At the current collectors tap walls, on the anodes side, a zero potential is forced, on the cathode side, a current flux was established. The constant current load simulates the in-series connection of the stack to build up the potential value. Constant velocity, temperature, and gas composition boundary conditions were formed at the inlets of flow channels. A

943

Table 1: Operating parameters applied for all stack configuration options comparison.

| Parameter	Value (Unit)
Inlets/furnace temperature	1173 (K)
Air flow rate	2 (L/min)
Hydrogen flow rate	1 (L/min)

constant atmospheric pressure and furnace temperature were applied to the channels outlets.

The numerical modeling was conducted using the SIMPLE scheme with the Richie-Chow distance-based flux type. Different spatial discretization methods were used to compute each parameter. Green-Gauss Node-Based method was used to calculate gradient, pressure was computed using Second Order spatial discretization method. Density, momentum, energy, species, and potential equations were computed using First-Order Upwind spatial discretization.

In order to conduct a comparison of each design shown in Fig. 2, a series of simulations were performed. To obtain current-voltage and current-power characteristics, an electric load in the form of a constant current was applied to the cathodes current collectors in the value from zero until the power drop. To validate the model, a comparison of electrical characteristics, obtained from the numerical simulation and the experimental study [11], was presented in Fig. 4. The operating parameters of the simulations were fitted to the parameters used during the experimental study. The experimental points with error bars included are presented in the form of circles, triangles and deltiods. The numerical analysis results are presented as solid, dashed, and dotted lines. The numerical model introduced in this paper allows to simulate highly predictable characteristics, which is confirmed in the comparison contained in Fig. 4. During the analysis, the lack of fuel and air was clearly visible, so the decision to increase the flow rates was made. The hydrogen flow rate was increased ten times and the air flow rate twenty times. The comparison of electrical characteristics obtained during numerical analysis, for flow rates tested during the experimental study and increased as mentioned above, is presented in Fig. 5. The solid lines represent the characteristics for flow rates as experimentally tested, and the dashed lines represent the characteristics for increased flow rates. It clearly revealed the gain in power in the value of 27.4 percent, from $P = 0.935$ W at a current of $I = 0.356$ A up to $P = 1.191$ W at $I = 0.515$ A. In order to conduct a reasonable comparison of each presented in Fig. 2 design, including the multistack design that consists of twelve cells, the increased flow rates remained constant for the whole further study. The operating parameters for the study of different designs, applied for all cases, are presented in Table 1.

To clarify the comparison of the performance of each design, four different graphs were shown in Fig. 6. For reference, the marks (a), (b1), (b2), and (c) are consistent with the geometries shown in Fig. 2. The first graph of Fig. 6 illustrates the current-voltage and current-power characteristics of case (a) and (b1), so the comparison of half-tubular and rectangular covers, with the electrolyte of 0.3 mm of thickness. The second graph presents the comparison of the characteristics of the initial case (a) and the design with rectangular shape of covers with reduced electrolyte thickness up to 0.1 mm (b2). The third plot presents a comparison of the performance of the initial case (a) and the multi-stack design (b), which consists of 12 cells. To better illustrate the performance comparison of four cases (a), (b1), (b2) and (c), a bar plot of the peak power density, located at the bottom of Fig. 6, was presented. Between the (a) and (b1) cases, the difference is almost unrecognizable, flattening the channels by changing the shape to rectangular resulted in the power drop from 1.19 W (a) to 1.16 W (b1). Reducing the electrolyte thickness resulted in an increase in the performance, as expected, due to an enhancement of electrolyte ionic conductivity. The power of case (b2) reaches 1.46 W. Multistack design (c) is clearly the most powerful arrangement option, power reaches the value of 2.87 W, but the power density is slightly lower than the case (b2). Furthermore, in the (c) case, a concentration loss at the characteristics is clearly visible, which could mean insufficient hydrogen supply, due to doubling of the number of cells, which could be a reason for the drop in power density. Moreover, at this it is worth to underline that the multi-stack design (c) volume is still reduced compared to the initial design (a), so the volumetric power density, which considers whole system volume, would increase.

Comparison of the temperature distribution, shown in Fig. 7, was presented to compare the inspected geometries in terms of heat transfer. The (a), (b1), (b2) and (c) design marks are consistent with geometries shown in Fig. 2. The temperature scale for each case was set as a global range to visualize the differences between cases. The initial design (a), as well as designs (b1) and (b2), are co-flow arranged, flow direction from left to right. The multistack design cross-flow is shown in Fig. 3 (fuel flow according to x-axis, air flow opposite to the z-axis). The distributions illustrated in Fig. 7, are shown in the form of semi-transparent shadow, where the minimum value is fully transparent and the maximum value is opaque. Each distribution was presented for the peak power point, determined during the study of electric characteristics. The temperature distribution does not change meaningfully between (a) and (b1), for both cases, peak power retains the same value of
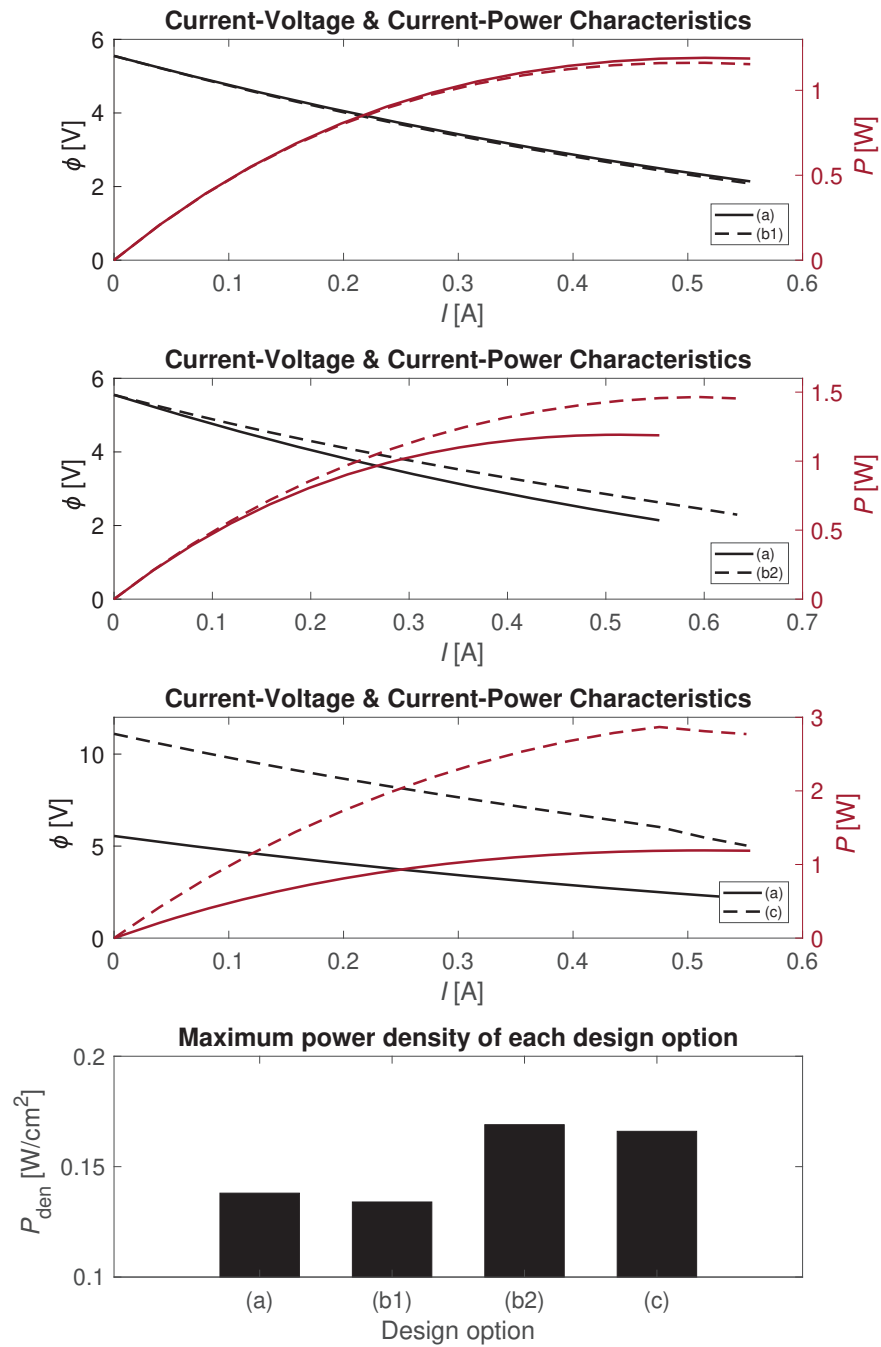
Figure 6: Comparison of current-voltage and current-power characteristics of four different designs, with a bar plot illustrating power density peak of each. Design marks (a), (b1), (b2) and (c) are consistent with geometries shown in Fig. 2.
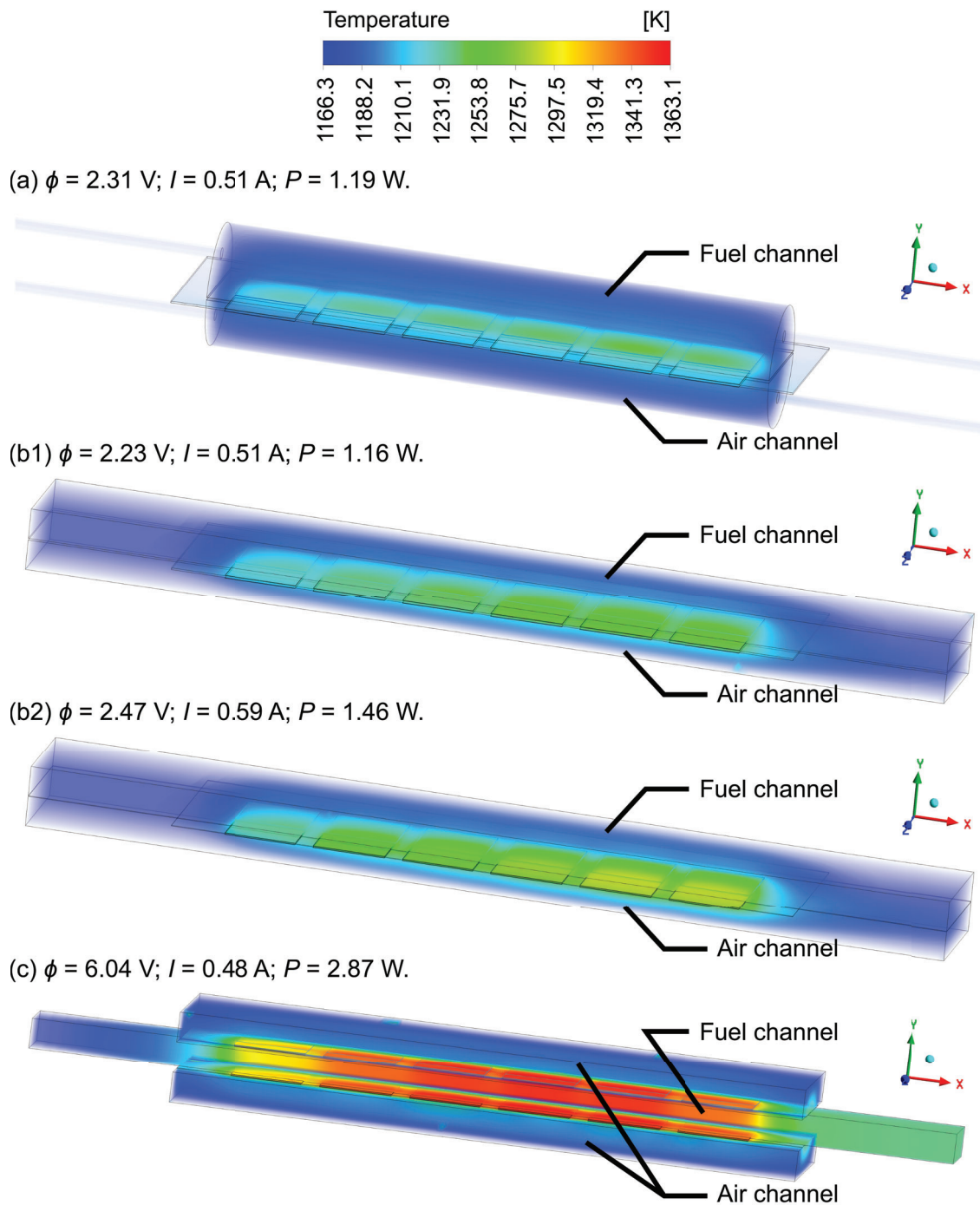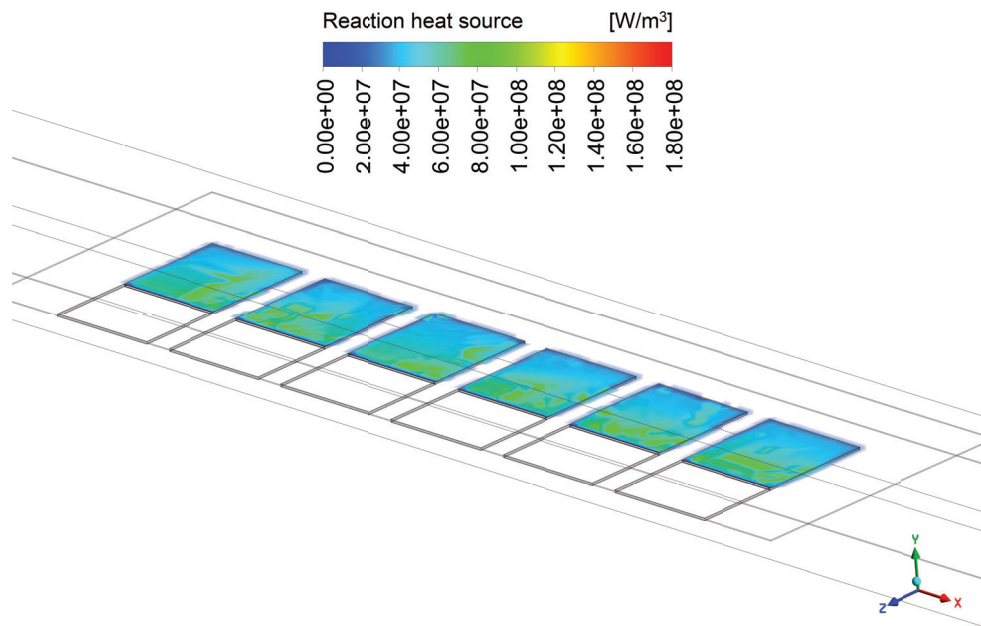
Figure 7: The temperature distribution comparison of peak power point of each inspected geometry. Design marks (a), (b1), (b2) and (c) are consistent with geometries shown in Fig. 2. The cases (a), (b1) and (b2) are co-flow formed, flow direction determines the *x*-axis. The (c) case cross-flow was shown in Fig. 3. Distribution in the form of semi-transparent shadow (min. value - transparent, max. value - opaque).

current. After implementing a thinner electrolyte (b2), the increase in current allowed the power peak to rise. Due to a higher load, a significant temperature increase occurs. The analysis of the multi-stack design reveals a major temperature increase in the fuel channel, between two sets of anodes. The interaction between both
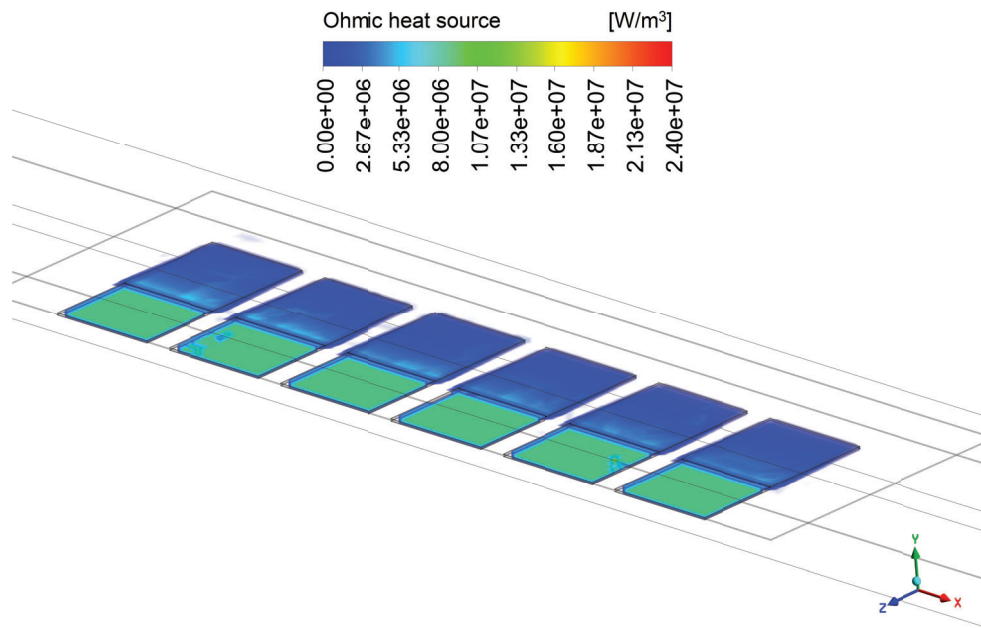
Figure 8: Ohmic heat source distribution in porous electrodes and current collectors, in the form of semi-transparent shadow (min. value - transparent, max. value - opaque). Design (b2), as shown in Fig. 2. Isometric view from the anode side. The flow direction determines the *x*-axis.
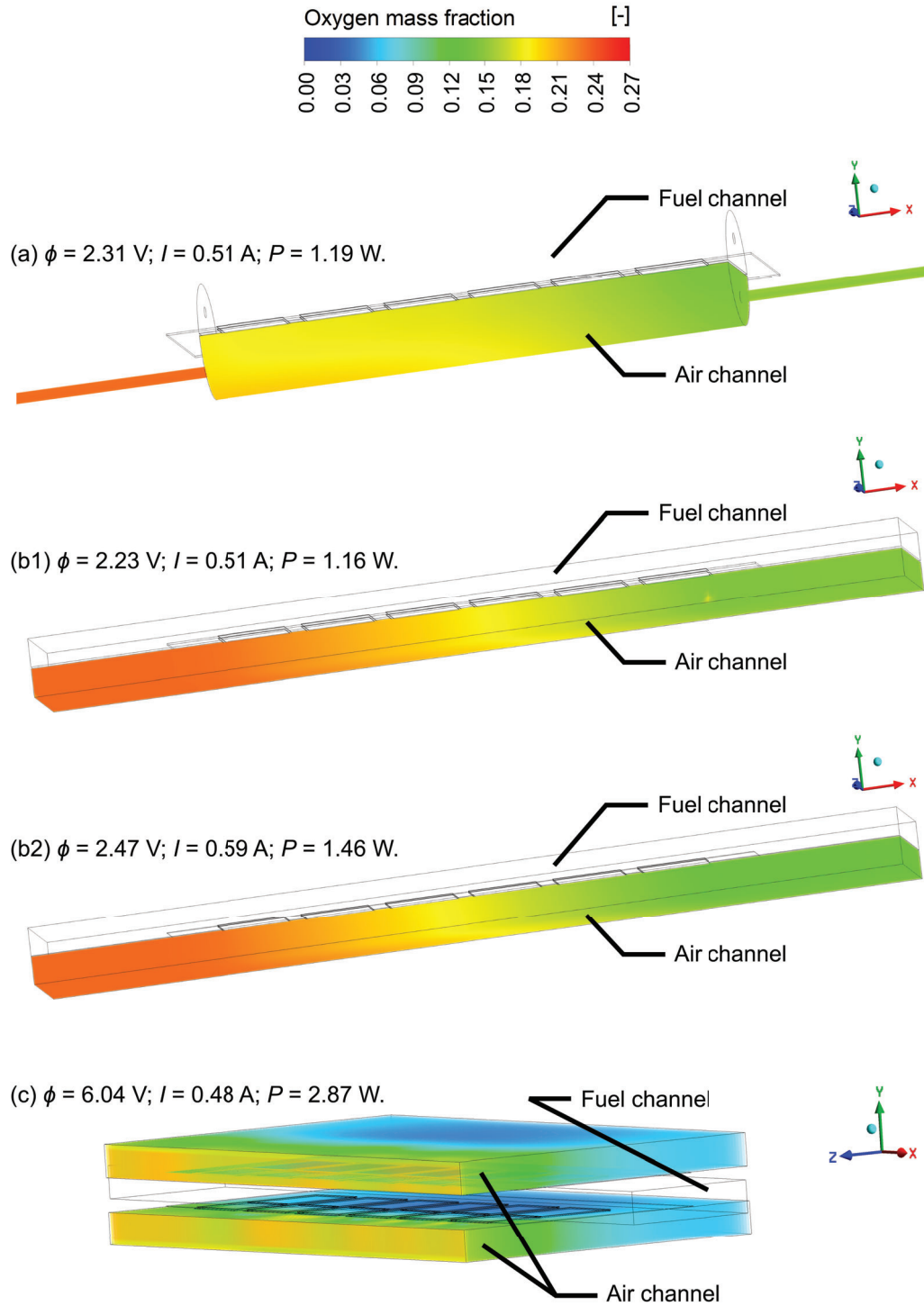

Figure 9: Reaction heat source distribution in porous electrodes, in the form of semi-transparent shadow (min. value - transparent, max. value - opaque). Design (b2), as shown in Fig. 2. Isometric view from the anode side. The flow direction determines the *x*-axis.
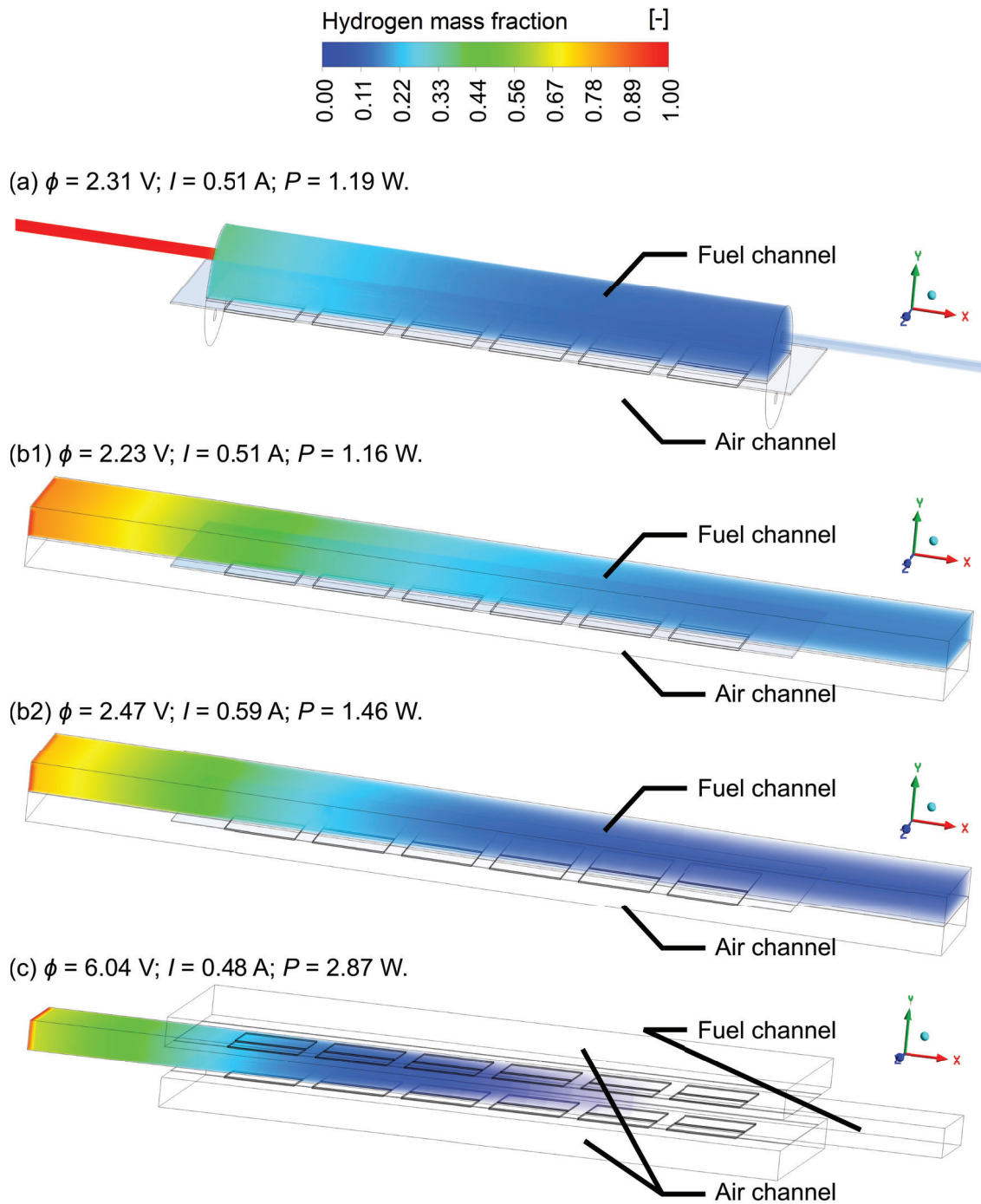
Figure 10: The hydrogen mass fraction distribution comparison of peak power point of each inspected geometry. Design marks (a), (b1), (b2) and (c) are consistent with geometries shown in Fig. 2. The cases (a), (b1) and (b2) are co-flow formed, flow direction determines the x-axis. The (c) case cross-flow was shown in Fig. 3. Distribution in the form of semi-transparent shadow (min. value - transparent, max. value - opaque).

stacks in the form of the generated, due to the electrochemical reaction and electrons/ions transport, heat, is clearly visible in the temperature distribution. From the outside, the constant temperature boundary condition cools the neighboring areas. The distribution analysis suggests that a multi-stack prototype could remain op-

Oxygen mass fraction [-]

0.00 0.03 0.06 0.09 0.12 0.15 0.18 0.21 0.24 0.27

(a) ϕ = 2.31 V; I = 0.51 A; P = 1.19 W.

Fuel channel

Air channel

(b1) ϕ = 2.23 V; I = 0.51 A; P = 1.16 W.

Fuel channel

Air channel

(b2) ϕ = 2.47 V; I = 0.59 A; P = 1.46 W.

Fuel channel

Air channel

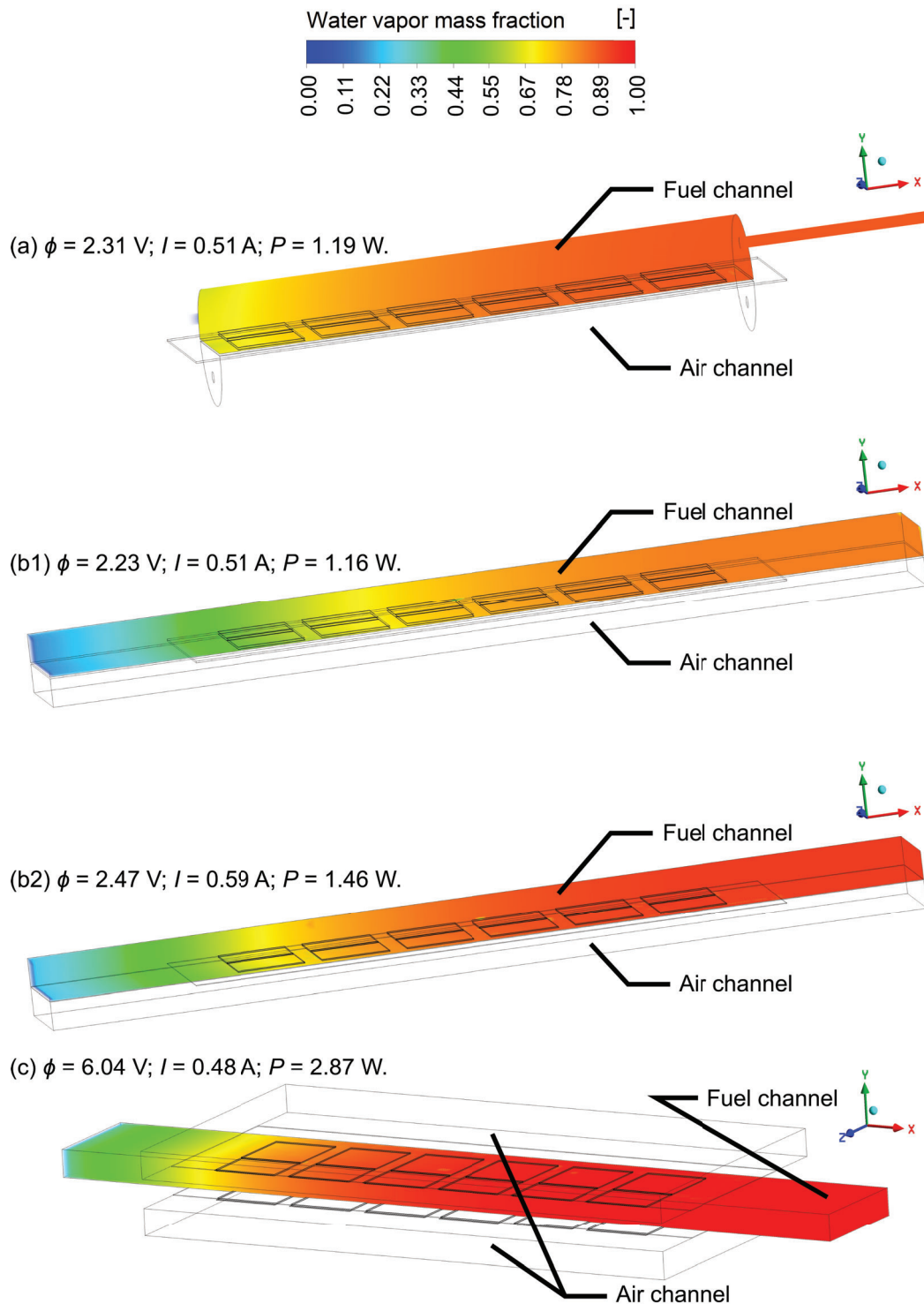(c) ϕ = 6.04 V; I = 0.48 A; P = 2.87 W.

Fuel channel

Air channel

Figure 11: The oxygen mass fraction distribution comparison of peak power point of each inspected geometry. Design marks (a), (b1), (b2) and (c) are consistent with geometries shown in Fig. 2. The cases (a), (b1) and (b2) are co-flow formed, flow direction determines the x-axis. The (c) case cross-flow was shown in Fig. 3. Distribution in the form of semi-transparent shadow (min. value - transparent, max. value - opaque).

Figure 12: The water vapor mass fraction distribution comparison of peak power point of each inspected geometry. Design marks (a), (b1), (b2) and (c) are consistent with geometries shown in Fig. 2. The cases (a), (b1) and (b2) are co-flow formed, flow direction determines the *x*-axis. The (c) case cross-flow was shown in Fig. 3. Distribution in the form of semi-transparent shadow (min. value - transparent, max. value - opaque).

erating temperature with low input of furnace heating. The heat sources distributions are presented in Fig. 8 and Fig. 9, for ohmic and reaction heat sources, respectively. The distributions are illustrated in the form of semi-transparent shadow, similar to a temperature distribution. The case chosen to illustrate the heat sources is the (c) design (as shown in Fig. 2), due to the highest power density, as shown in Fig. 6. The flow direction is in accordance with the x-axis. The range of values is global, so the maximum visible value is the highest observed. As illustrated, the greatest impact on temperature rise has the reaction heat source, shown in Fig. 8, where the values remain an order of magnitude higher compared to the ohmic heat source, shown in Fig. 9.

The distributions of the mass fractions of hydrogen in the fuel channel, oxygen in the air channel, and water vapor in the fuel channel are illustrated in Fig. 10, Fig. 11 and Fig. 12, respectively. The distributions are presented in the form of semi-transparent shadow, where minimum values are fully transparent, and maximum values are opaque. The (a), (b1), (b2) and (c) design marks are consistent with geometries shown in Fig. 2. The scales for each case were set as global ranges to visualize the differences between cases. The initial design (a), and the designs (b1) and (b2) are co-flow arranged, flow direction in accordance with the x-axis. The multi-stack design cross-flow is illustrated in Fig. 3, where fuel flows according to x-axis and air in the opposite way to the z-axis. The distribution of the hydrogen mass fraction reveals the proper reaction of the model, while the comparison of (a) design and (b1) design does not give clear changes, between (b1) and (b2), the influence of changing the electrolyte thickness and simultaneously increasing the power, presents a visible difference. The case (b2) compared to (b1) utilizes much more fuel compared to the case (b1). In the (c) case, the fuel supply is utilized in full measure, so it is expected that the power density was lower than in (b2) due to the lack of fuel, especially counting the higher operating temperature in (c), which should result in higher performance. The high level of concentration loss in the (c) case is also visible in Fig. 6. The current load value in (c) case is also lower at the power peak point than in (b2), so the increase in fuel supply should yield in performance increase, and allow to apply load similar to (b2). The oxygen mass fraction illustrates the assumed surplus of air flow rate in all studied cases. The difference between the (a), (b1), and (b2) cases is subtle, the main difference is visible in the (c) case, due to doubling of cells amount, but still remaining some margin of oxygen. The water vapor mass fraction distribution also presents the proper operation of the model. After the oxygen and hydrogen are consumed, steam is produced and gradually fulfills the fuel channels. The steam mass fraction in cases (a) and (b1) remains at a similar level. After the increase in load and power gain, due to the decrease in the thickness of the electrolyte in case (b2), hydrogen and oxygen are consumed in greater amounts and the increase in steam generation is clearly visible. In the (c) case, the multistack generates the steam the most heavily and the value of steam mass fraction remains high since the first cells, while in the last cells area the water vapor fulfills the channel entirely.

5. Conclusions

This paper has provided an important analysis, in terms of further prototyping, of the novel banded SOFC stack. Four different geometries were designed as CAD models to include the influence of the configuration of the stack system on the performance. Also, different electrolyte thickness values were modeled. The computational mesh of each design was established to provide a domain for the finite-volume computation method. The mesh size was a result of the mesh sensitivity study to complete the requirements of high precision of the solution, high resolution, and reasonable computational time. As presented, the meshes were formed to fulfill the mentioned requirements, by forcing the elements dimensions changes in crucial areas. To understand the conducted research, a mathematical model was described, including implementing the model into the numerical analysis.

The main goal of this research was to inspect the performance changes. To validate the model for different gas flow rates, a comparison of electrical characteristics obtained from numerical analysis with experimental study results was performed and revealed the high level of predictability of the model. In order to obtain a proper comparison of different designs, including changes in the air and fuel channels, the electrolyte thickness, and the method of multistacking, the flow rates were set to higher value to maintain a surplus. To illustrate the results of the comparison, current-voltage and current-power characteristics were studied. Each design presented a response to applied modifications. The whole process of modification, from initial single stack with half-tubular covers design, to the final multi-stack design resulted in the performance increase of 141.2 %, from 1.19 W up to 2.87 W, while maintaining a comparable volume of the system. The multi-stack design proved to be the right way of extending the stack design into a bigger system. An arrangement of joining two stacks to one fuel channel, established partially by the stacks themselves, in terms of extending the system size, can double the power of the system without increasing the volume. Moreover, realizing the air supply as the side fan could significantly simplify the initial design. Temperature distribution analysis revealed another advantage of multistacking method as proposed. The neighboring stacks heat up each other, which in the prototype scale, could allow to minimize furnace input, and in the commercial scale, could enforce cooling the system, by fitting the gases flow rates. The full analysis of transport phenomena was performed including heat, mass, and electron transport. The results of hydrogen distribution exposed the lack of fuel in the multistack design, so the

https://doi.org/10.52202/069564-0085

final gain in power could be even higher than presented. The influence of load on transport phenomena was illustrated and inspected. In comparison of the studied stack with conventional, commercial-like designs the power density is not impressive, the highest power density value obtained during this study was $0.17\,\mathrm{W\,cm^{-2}}$, while it is common to reach values over $0.5\,\mathrm{W\,cm^{-2}}$ [9], so there is much space for further improvements.

In the future, the developed simulation can be used to analyze electrolyte and electrodes geometry and current collectors arrangement, allowing the construction of new and improved stack versions. Moreover, after contributing a new method of extending the single-stack system into a multistack, an analysis of the extended-scale fuel supply system in terms of fluid mechanics can be conducted. The model can also be used to analyze the influence of materials improvements by conducting material and electrochemical parametric studies, such as the impact of the electrolyte conductivity on performance, since it is considered as one of the most important parameters for this kind of stack.

Acknowledgments

Nomenclature

Letter symbols

F Faraday constant, $(9.65 \times 10^7\,\mathrm{C\,mol^{-1}})$

h specific enthalpy, $(\mathrm{J\,kg^{-1}})$

h_{react} enthalpy change, $(\mathrm{J\,mol^{-1}})$

I current, (A)

$i_{\mathrm{an}}^{\mathrm{eq}}$ anode equilibrium exchange current, $(\mathrm{A\,m^{-1}})$

$i_{\mathrm{cat}}^{\mathrm{eq}}$ cathode equilibrium exchange current, $(\mathrm{A\,m^{-2}})$

i current density flux, $(\mathrm{A\,m^{-2}})$

j volumetric transfer current density, $(\mathrm{A\,m^{-3}})$

$\vec{J}_i$ diffusion flux, $(\mathrm{kg\,m^{-2}\,s^{-1}})$

k thermal conductivity, $(\mathrm{W\,m^{-1}\,K^{-1}})$

M molar mass, $(\mathrm{kg\,mol^{-1}})$

p static pressure, (Pa)

P power, (W)

P_{den} power density, $(\mathrm{W\,cm^{-2}})$

R universal gas constant, $(8.314\,\mathrm{J\,K^{-1}\,mol^{-1}})$

$\vec{S}$ source/sink term of momentum, $(\mathrm{kg\,m^{-2}\,s^{-2}})$

S_h source/sink term of heat, $(\mathrm{W\,m^{-3}})$

S_i source/sink term of species rates, $(\mathrm{kg\,m^{-3}\,s^{-1}})$

S_p source/sink term of mass, $(\mathrm{kg\,m^{-3}\,s^{-1}})$

T temperature, (K)

$\vec{v}$ velocity vector, $(\mathrm{m\,s^{-1}})$

X_i local species concentration, $(\mathrm{kmol\,m^{-3}})$

Y_i species mass fraction, (-)

Greek symbols

α transfer coefficient, (-)

γ concentration dependence, (-)

ε porosity rate, (-)

ζ_{TPB} triple phase boundary length density, ($m\,m^{-3}$)

ζ_{DBP} double phase boundary length density, ($m^2\,m^{-3}$)

η local surface overpotential, (V)

ρ density, ($kg\,m^{-3}$)

σ conductivity, ($S\,m^{-1}$)

$\bar{\bar{\tau}}$ stress tensor, (Pa)

ϕ potential, (V)

Subscripts and superscripts

a   anodic

an   anode

c   cathodic

cat   cathode

den   density

DPB   double phase boundary

eff   effective value

el   electronic

eq   equilibrium

i reaction component

ion   ionic

ref   reference value

s   solid

react   reaction

TPB   triple phase boundary

Abbreviations

3D   three-dimensional

CAD   computer aided design

CFD   computational fluid dynamics

OCV   open circuit voltage

SOFC   solid oxide fuel cell

References

[1] Buchaniec S., Sciazko A., Mozdzierz M., Brus G. *A Novel Approach to the Optimization of a Solid Oxide Fuel Cell Anode Using Evolutionary Alghorithms.* IEEE Access 2019;7:34361-34372.

[2] Ghorbani B., Vijayaraghavan K. *A review study on software-based modeling of hydrogen-fueled solid oxide fuel cells.* International Journal of Hydrogen Energy 2019;44:13700-13727.

[3] Mozdzierz M., Berent K., Kimijima S., Szmyd J.S., Brus G. *A Multiscale Approach to the Numerical Simulation of the Solid Oxide Fuel Cell.* Catalysts 2019;9/253.

[4] Pianko-Oprych P., Zinko T. *Simulation of the steady-state behaviour of a new design of a single planar Solid Oxide Fuel Cell.* Polish Journal of Chemical Technology 2016;1:64-71.

[5] Pianko-Oprych P., Zinko T. *Computational fluid dynamics calcultion of a planar solid oxide fuel cell design running on syngas.* Chemical and Process Engineering 2017;38:513-521.

[6] Chalusiak M., Wrobel M., Mozdzierz M., Berent K., Szmyd J.S., Kimijima S., Brus G. *A numerical analysis of unsteady transport phenomena in a Direct Internal Reforming Solid Oxide Fuel Cell.* International Journal of Heat and Mass Transfer 2019;131:1032-1051.

[7] Wei S.S., Wang T.H., Wu J.S. *Numerical modeling of interconnect flow channel design and thermal stress analysis of a planar anode-supported solid oxide fuel cell stack.* Energy 2014;69:553-561.

[8] Dong S.-K., Jung W.-N., Rashid K., Kashimoto A. *Design and numerical analysis of a planar anode-supported SOFC stack.* Renewable Energy 2016;94:637-650.

[9] Pirasaci T. *Non-uniform, multi-stack solid oxide fuel cell (SOFC) system design for small system size and high efficiency.* Journal of Power Sources 2019;426:135-142.

[10] Brus G. *High-Temperature Solid Oxide Fuel Cell Stack* International Claim no. H01M 8/2432 (2016.01), H01M 8/2475 (2016.01).

[11] Chalusiak M. *Development of solid oxide fuel cell manufacturing methodology using 3D printing technique.* PhD dissertation. Krakow, Poland: AGH University of Science and Technology; 2023.

[12] Mukerjee S., Leah R., Selby M., Stevenson G., Brandon N. P. *Chapter 9 - Life and Reliability of Solid Oxide Fuel Cell-Based Products: A Review.* In: Brandon N. P., Ruiz-Tjero E., Boldrin P. editors. Solid Oxide Fuel Cell Lifetime and Reliability. London, UK: Academic Press. 2017. p. 173-191.

[13] Prokop T.A., Berent K., Iwai H., Szmyd J.S. *A Three-Dimensional Numerical Assessment of Heterogeneity Impact on a Solid Oxide Fuel Cell's Anode Performance.* Catalysts 2018;8:503.